MATERIALS SCIENCE

Self-powered enzyme-linked microneedle patch for scar-prevention healing of diabetic wounds

Xiangli Zhang[1], Zhilong Wang[1], Hong Jiang[1], Huajing Zeng[1], Nan An[1], Bin Liu[1]*, Luyi Sun[2]*, Zengjie Fan[1]*

Diabetic wounds with complex pathological features and a difficult-to-heal nature remain a formidable challenge. To address this challenge, we design and fabricate a self-powered enzyme-linked microneedle (MN) patch composed of anode and cathode MN arrays, which respectively contain glucose oxidase (GOx) and horseradish peroxidase (HRP) encapsulated in ZIF-8 nanoparticles. The enzymatic cascade reaction in the MN patch can effectively reduce local hyperglycemia in diabetic wounds while generating stable microcurrents to promote rapid healing of diabetic wounds. Therefore, the diabetic wounds treated with this MN patch exhibit rapid, complete, and scar-preventative healing, which can be attributed to the synergistic actions of hypoglycemic, antibacterial, anti-inflammatory, and bioelectrical stimulation. In brief, the self-powered MN patch is an effective method to rapidly promote diabetic wound healing and prevent scar formation.

INTRODUCTION

Because of local hyperglycemia, chronic inflammation, and repeated infection, diabetic wounds typically have the problems of limited treatment effect and prolonged healing, which seriously affect the daily life of patients, and even cause the risk of amputation (*1*). Traditional wound dressings and hydrogel wound dressings are commonly used to treat diabetic wounds. Although they have made notable advancements in promoting wound healing, the existing disadvantages, including single function, limited repair effect, and secondary trauma caused by peeling the adhesive dressings from the wounds, remain unsolved (*2*, *3*).

With the advancement of micro-nano fabrication, a new treatment method based on microneedle (MN) technology has been developed. An MN patch consists of an array of needle tips with a length of around 10 to 2000 μm and a diameter of less than 300 μm (*4*). MN is minimally invasive, painless, and convenient. As a transdermal delivery method, MN has found wide research in diabetic wounds. What is more, an MN patch can attach itself to the wound surface by mechanical interlocking to avoid suture trauma (*5*). Recently, researchers have developed various MNs, including drug delivery MNs, growth factor–releasing MNs, and nitric oxide (NO)–releasing MNs, to treat diabetic wounds and achieved a promising therapeutic effect on diabetic wounds (*6*–*8*). However, few studies based on MNs can effectively prevent scarring.

Until now, the mechanism of scar formation remains obscure. It is believed that the overproduction of fibroblasts and the disappearance of bioelectricity around the wound are probably the main reasons (*9*, *10*). Bioelectricity, in particular, gradually weakens or even disappears during the slow process of wound repair, which causes disordered regulation of wound repair genes and down-regulation of wound-healing cascades, resulting in disordered collagen fiber deposition and abnormal remodeling extracellular matrix (ECM), eventually leading to the formation of scar (*11*, *12*).

Therefore, how to stimulate and amplify endogenous bioelectricity has become a research hotspot in the field of tissue repair. The development of piezoelectricity and triboelectrification technology provides a new avenue to stimulate the generation of endogenous bioelectricity (*13*, *14*). However, the bioelectricity stimulated by this technology has the disadvantages of being unstable and unsustainable. The external power supply can overcome these drawbacks, but the inconvenience of carrying and using an external power supply limits its usage in wound management (*15*–*17*). Compared to the above-mentioned methods, enzymatic biofuel cells (BFCs) can use biological enzymes as highly efficient electrocatalysts to convert chemical substances such as blood glucose and lactic acid in living organisms into the stable and continuous current and have the advantage of miniaturization, portability, low production cost, green, and good biocompatibility (*18*). Therefore, BFCs have gotten wide applications in the field of medical electronic implants such as pacemakers, deep-brain nerve stimulators, and insulin pumps (*19*).

As one of the most common of the BFCs, glucose BFCs, have found wide applications in vivo, thanks to the following substantial advantages (*18*–*20*): (i) The utilization of natural bioenzymes will not have any toxicity effect on human health. (ii) The anode containing glucose oxidase (GOx) will consume glucose to generate electricity, thus decreasing the glucose concentration around the wound. (iii) The oxygen produced from the cathode contains horseradish peroxidase (HRP) will benefit wound healing (*21*). (iv) Owing to the ample glucose supply, stable and continuous bioelectricity can be continuously output. Furthermore, the integration of BFCs with MN will provide a simple and efficient approach to wound management.

The cascade reaction between GOx and HRP will ensure a highly efficient current output, which can provide endogenous bioelectricity to promote wound healing and prevent scarring. However, free enzymes have disadvantages of poor stability, easy inactivation and denaturation, low reuse rate, difficult reaction control, and unsatisfactory catalytic effect, which make the operation of a dual-enzyme system complicated and expensive, thus limiting its long-term

[1]Key Laboratory of Dental Maxillofacial Reconstruction and Biological Intelligence Manufacturing, Gansu Province, School of Stomatology, Lanzhou University, Lanzhou 730000, P.R. China. [2]Polymer Program, Institute of Materials Science and Department of Chemical and Biomolecular Engineering, University of Connecticut, Storrs, CT 06269, USA.
*Corresponding author. Email: liubkq@lzu.edu.cn (B.L.); luyi.sun@uconn.edu (L.S.); zjfan@lzu.edu.cn (Z.F.)

development (*22*, *23*). The zeolite imidazolate framework (ZIF-8) is a polyhedron with a rough surface, which has the advantages of ease of synthesis, high stability, large specific surface area, and high porosity (*24*, *25*). Therefore, ZIF-8 is widely used to immobilize and protect bioactive ingredients, such as enzymes, proteins, DNA, and so on (*26*–*29*). In addition, ZIF-8 has been certified effective in terms of its antibacterial activity, which can protect the wound from bacterial infections (*30*, *31*).

Here, in this study, we designed and prepared a self-powered enzyme-linked MN patch by combining the MN technology and BFCs. The prepared MN patch consisted of conductive anode and cathode arrays, which can produce a stable and lasting current by consuming blood glucose, enabling to reduce blood glucose concentration around the wound (Fig. 1). In addition, it showed excellent antibacterial properties, high biocompatibility, and efficient inflammatory inhibition. The wound treated with this MN patch exhibited rapid and scar-prevention healing, indicating its therapeutic potential for diabetic wounds.

RESULTS AND DISCUSSION

Characterization of DA-PPy

The high conductivity of the MN patch can reduce the transport resistance of electrons, enabling an efficient and durable current generation of BFCs. Here, we chose polypyrrole (PPy) as the conductive material to improve the conductivity of the MN patch because of its high conductivity and low cytotoxicity (*32*, *33*). However, the poor dispersion of PPy in water limits its usage. As reported, dopamine (DA) modification is an effective method to improve the dispersion of PPy (*34*). Accordingly, we used DA to modify PPy to prepare DA-PPy, and the results showed that the PPy modified by DA can ensure a good dispersion in water (fig. S1). In addition, the surface morphology was characterized by scanning electron microscopy (SEM; Fig. 2A). One can observe that the modification with DA can change the morphology of PPy from clustered particles to short fiber-like structures.

Besides the morphological characterization, the successful synthesis of DA-PPy can be confirmed by Fourier transform infrared (FTIR; fig. S2A). In PPy, the bands at 1534 and 1594 cm^{-1} can be assigned to the C—C and C═C stretching vibration of the pyrrole ring, respectively, while the band at 1451 cm^{-1} can be attributed to the C—N stretching vibration. In addition, the C—H stretching vibration peaks of the pyrrole ring appeared at 1170 and 1310 cm^{-1}. After the in situ polymerization of pyrrole and DA to synthesize DA-PPy, the characteristic band of DA at 2930 cm^{-1} can be also observed in addition to the characteristic peak of PPy.

Characterization of ZIF-8 and its enzyme composites

ZIF-8, ZIF-8–containing GOx (denoted as ZG), and ZIF-8–containing HRP (denoted as ZH) nanoparticles were successfully synthesized according to the reported method (*35*) and characterized by transmission electron microscope (TEM). As shown in Fig. 2

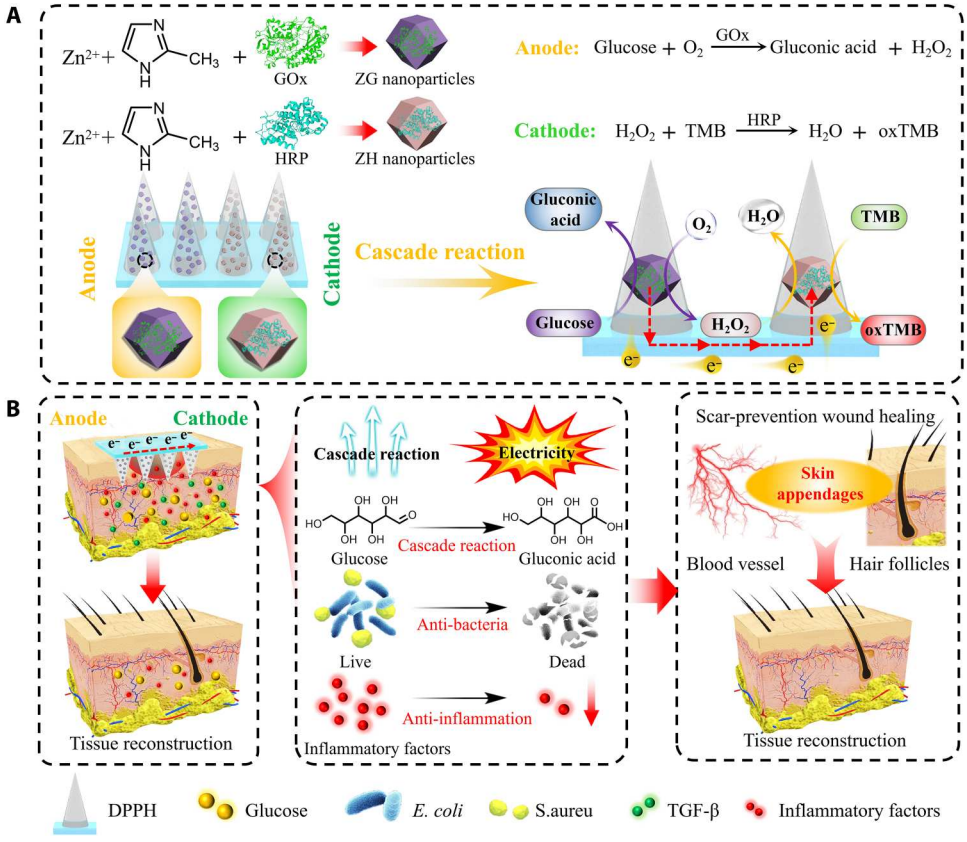

Fig. 1. Schematic diagram of self-powered MN patch. (**A**) Schematic of the enzyme cascade reaction generated by the self-powered MN patch. (**B**) Schematic of the self-powered enzyme-linked MN patch for accelerating diabetic wound healing.

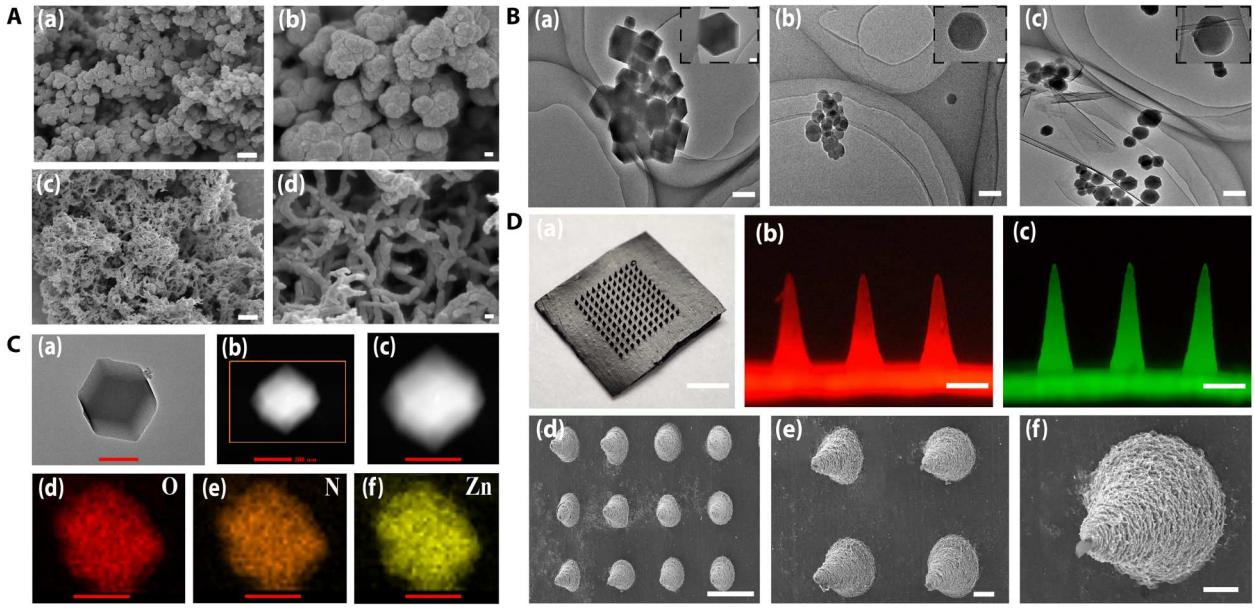

Fig. 2. Surface morphology analyses of the synthesized materials and MN patches. (**A**) SEM images of (a and b) PPy and (c and d) DA-PPy [scale bars, 100 nm (b and d) and 1 μm (a and c)]. (**B**) TEM images of (a) ZIF-8, (b) ZG, and (c) ZH [scale bars, 200 nm (a), 500 nm (b and c), and 50 nm in the inset]. (**C**) TEM and EDS images of ZIF-8 (scale bars, 200 nm). (**D**) Materials and morphology of the MNs: (a) Optical image of the MN patch (scale bar, 2.5 mm). (b and c) Fluorescence microscopic images of the tip-loaded RhB and fluorescein (scale bars, 200 μm). (d to f) SEM images of the MNs [scale bars, 500 μm (d), 100 μm (e), and 50 μm (f)].

[B and C (a)], ZIF-8 has a dodecahedral structure with regular morphology and uniform size. However, the introduction of two kinds of enzymes changed its morphology from dodecahedral to spherical particles with a rougher surface. This change is believed to be owing to the competitive coordination between the enzyme and the defective site of the imidazole group (*36*). Energy-dispersive spectroscopy (EDS) mapping reveals homogeneous distributions of oxygen, nitrogen, and zinc elements of ZIF-8 [Fig. 2C (d to f)].

To confirm the successful synthesis of ZIF-8 and its enzyme composites, we further characterized them by FTIR and x-ray diffraction (XRD). In fig. S2B, one can observe that ZIF-8 has an N—Zn vibration peak, C═N stretching vibration peak, and C—N stretching vibration peak appeared at 995, 1430, and 1150 cm^{-1}, respectively. For the ZIF-8/enzyme composites, the characteristic peaks of GOx and HRP also appeared, which proves that ZIF-8/enzyme composites were successfully synthesized. Meanwhile, the characteristic peaks of DA-PPy and ZIF-8 could be observed in the composite of DA-PPy/polyvinyl alcohol (PVA)/hyaluronic acid (HA) (DPPH) conductive substrate, indicating that DA-PPy and ZIF-8 were successfully introduced into DPPH. In addition, the phase composition of the synthesized ZIF-8 and its enzyme composites were characterized by XRD (fig. S2C). The results showed that the synthesized ZIF-8 had a similar pattern to its simulated one, confirming the successful synthesis of ZIF-8. Moreover, the diffraction peaks of ZG and ZH nanoparticles were the same as the ones of ZIF-8, suggesting that the introduction of enzymes did not change the structure of ZIF-8. Furthermore, we used a BCA (bicinchoninic acid) protein quantification kit to make a quantitative analysis of the loading amount of the two kinds of enzymes. The results showed that the enzyme loading amount of GOx and HRP in ZIF-8 nanoparticles were 87.47 and 87.52%, respectively (fig. S2, D and E).

Evaluation of enzyme activity

To evaluate the enzymatic activities of GOx and HRP in ZIF-8 nanoparticles, we catalyzed a cascade reaction using 3,3′,5,5′-tetramethylbenzidine (TMB) and glucose (Glu) as the colorimetric substrates (*37*–*39*). The ultraviolet (UV)–visible characterization result showed that after the addition of Glu and TMB, ZG, ZH, and the free enzyme cascade samples all appeared with distinct peaks at the wave numbers of 370 and 652 nm (fig. S2F), which means that the enzyme cascade reaction was successfully triggered, and TMB was oxidized to oxTMB (a blue product with a characteristic peak at the wave number of 652 nm). After adding a small amount of H_2SO_4, the blue product was converted to a yellow product with a characteristic absorption peak at the wave number of 450 nm, confirming that the enzyme activities of the ZIF-8/enzyme composite were well maintained.

Characterization of the MN patches

In this study, a self-powered enzyme-linked MN for rapid diabetic wound healing was prepared by a two-step method (fig. S3). The MN patch is composed of an array of 11 × 11 MNs arranged in an orderly manner [Fig. 2D (a)]. As shown in Fig. 2D (b and c), rhodamine B (RhB) and green fluorescein were evenly distributed on the needle tip under the fluorescence microscope, verifying the loading capability of various drugs, as well as proteins owing to the porous structure of MNs [Fig. 2D (f)]. In addition, its morphology was imaged with SEM. One can observe that the needles are uniform cones arranged neatly and orderly on the substrate with a spacing of 300 μm, and each needle has a base diameter of 200 μm and a height of 600 μm [Fig. 2D (d to f)].

The hyperglycemic environment of diabetic wounds can trigger a rapid enzymatic cascade reaction of MNs, enabling to generate higher microcurrents to accelerate wound healing and potentially

prevent scar formation. Therefore, the self-powered features of the MNs were explored both in vitro and in vivo (fig. S4). In vitro, the microcurrents generated from the MNs by consuming different concentrations of glucose were detected using a high-precision benchtop digital multimeter. As shown in fig. S4A, the output current of the MNs presented an increasing trend corresponding to an increasing glucose concentration. When the glucose concentration was 0, 18, 20, 24, and 26 mM, the output current generated by the MNs was ±1.01, ±1.74, ±2.01, ±2.32, ±2.64, and ± 3.53 μA, respectively, indicating the high response of the MNs to different concentrations of glucose. In vivo, the MN patch was fixed to a diabetic wound, and the generated microcurrents were also detected by a high-precision benchtop digital multimeter. As shown in fig. S4B, compared to normal wounds, the local hyperglycemia of diabetic wounds can generate a higher and nonconstant current, probably because of the glucose consumption around the MN anode caused by the oxidase reaction between GOx and glucose to produce gluconic acid and hydrogen peroxide. Subsequently, a further study on the correlation between the glucose consumption and the output current was carried out by the linear regression analysis (fig. S4C). On the basis of this, the blood glucose concentration consumed by the enzyme-linked MN patch around the wounds can be quantified in a real-time way (*40*) (fig. S4D). As shown in fig. S4D, one can observe that the MN patch can consume more glucose in diabetic wounds than that in normal wounds, which is the reason for generating higher electricity. Although the glucose around the diabetic wounds can be consumed, dynamic blood circulation can partially replenish the consumed glucose. Therefore, the diabetic wounds will not appear the phenomenon of hypoglycemia, ensuring the secure application of the MNs in vivo.

Mechanical properties

The mechanical properties of the MNs were tested by a universal mechanical test machine. As shown in fig. S5 (A and B), with an increasing HA concentration, the mechanical strength of the MNs increased accordingly. With a displacement of 450 μm, the force can reach 30 N, sufficiently meeting the mechanical requirement for piercing the skin (*41*). In addition to the piercing capability, the catechol groups on the surface of DA-PPy can enhance the adhesion ability of the MNs to the wound tissue via the formation of hydrogen and covalent bonds with the wound tissue (*42*).

Antibacterial performance and biocompatibility

Bacteria are believed to be an important reason for the repeated infection of diabetic wounds. Therefore, the antibacterial ability of wound dressings is of great importance for the healing of diabetic wounds (*43*). In this study, different concentrations of ZIF-8, ZG, and ZH (0, 0.3, 0.5, and 1.0 mg/ml) nanoparticles were used to evaluate the antibacterial ability against *Escherichia coli* and *Staphylococcus aureus*. As shown in Fig. 3, the killing rate of *E. coli* and *S. aureus* increased notably when the concentration of all samples exceeded 0.3 mg/ml. When the concentration reached 0.5 mg/ml, the killing rate reached 100%, confirming their high antibacterial performance. Hence, the concentration of the nanoparticles used in the following MN preparation was 0.5 mg/ml.

Subsequently, the prepared MN patches were cocultured with *E. coli* and *S. aureus*, respectively, to evaluate the MN patches′ antibacterial ability. As shown in fig. S6, the killing rates of the blank-MN patch against *E. coli* and *S. aureus* was 49.1 and 71.2%, which was probably due to the electrostatic interaction between the DA-PPy nanoparticles and bacteria, resulting in the death of bacteria (*44*). However, when nanoparticles (0.5 mg/ml) were added to the preparation of MN patches, the bactericidal performances of the prepared MN patches were significantly increased, and the killing rate of all MN patches reached 100%, indicating that the prepared MN patches have excellent antibacterial properties.

Although ZIF-8 nanoparticles have an excellent antibacterial ability, high concentrations of Zn^{2+} are potentially toxic to cells. So, cytotoxicity tests of the ZIF-8 nanoparticles were performed using the 3-[4, 5-dimethylthiazol-2-yl]-2, 5-diphenyltetrazolium-bromide (MTT) method and live/dead cell staining (Fig. 4). During the whole culture process, the cell viability of all samples was equal to or higher than 85%, indicating that all MN samples had low cytotoxicity. In addition, the number of live cells (green) detected by live/dead cell staining was consistent with the results of MTT, further confirming their high biocompatibility.

Healing evaluation of diabetic wound in vivo

To evaluate the effect of the MN samples on promoting the healing of diabetic wounds, the established I diabetic rats through streptozotocin (STZ) induction were randomly divided into six groups with nine rats in each group, including (i) control group, the wound without any treatment; (ii) blank-MN group, the wound treated with the pure MN patch; (iii) ZIF-MN group, the wound treated with the MN patch containing ZIF-8 nanoparticles; (iv) ZG-MN group, the wound treated with the MN patch containing ZG nanoparticles; (v) ZH-MN group, the wound treated with the MN patch containing ZH nanoparticles; and (vi) ZGH-MN group, the wound treated with the enzyme cascade reaction MN patch that can generate microcurrents. Photographs of the wounds on days 7, 14, and 21 were taken for the analysis of the wound-healing rate (Fig. 5A). The results showed that the ZGH-MN group had the best effect on promoting wound healing. Quantitatively, the wound area was 16.6% in the control group, 9.3% in the blank-MN group, 6.0% in the ZIF-MN group, 0.4% in the ZG-MN group, 1.6% in the ZH-MN group, and 0% in the ZGH-MN group (Fig. 5B). The results of the animal experiments show that the ZGH-MN patch can effectively promote the healing of diabetic wounds.

Histological analysis

The self-powered enzyme-linked MN patch was proved to be effective in promoting diabetic wound healing and preventing scar formation. To investigate the biological mechanism of the diabetic wound-healing process, we used histochemical and immunohistochemical methods.

First, we observed and recorded the contraction of the wound beds and the progress of the epithelization by hematoxylin-eosin (H&E) staining, as shown in Fig. 5C. On the seventh day, the tissue defects in each group were obvious, and bacterial infection and accumulation of a large number of inflammatory cells that caused acute inflammatory response remained. However, the inflammatory response in the ZGH-MN treatment group was lighter than that of the other groups. On the 14th day, the cells in the wounds of each group proliferated greatly, the granulation tissue began to form, and the wounds partially healed. In the control group, the healing speed was much slower, and there were still large areas of tissue defects, while the wound areas in the treatment

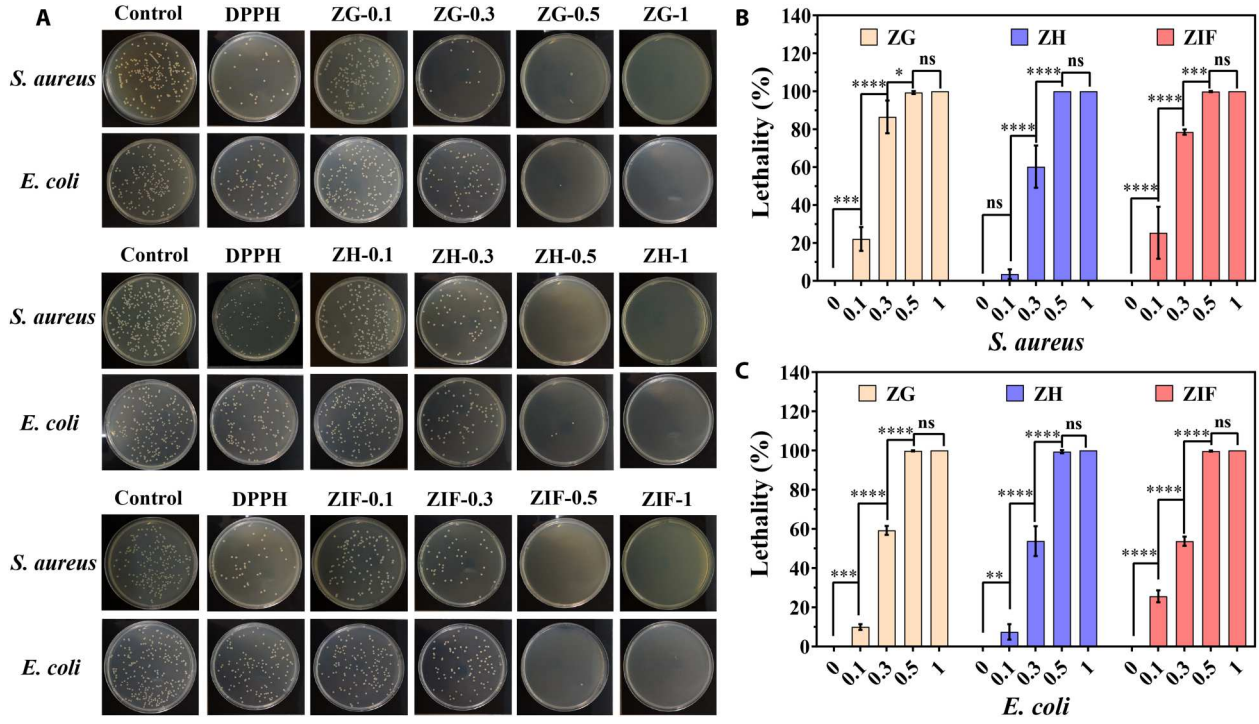

Fig. 3. Antibacterial test of the synthesized materials. (**A**) Photographs of different concentrations of ZIF-8 and ZG/ZH (0, 0.3, 0.5, and 1.0 mg/ml) nanoparticles against *E. coli* and *S. aureus*. (**B** and **C**) Statistics of the mortality of *S. aureus* and *E. coli* with different nanoparticle concentrations ($n = 3$ per group; significances are presented by $^{*}P < 0.05$, $^{**}P < 0.01$, and $^{***}P < 0.001$; ns, not significant).

groups were significantly reduced. In the group treated with ZGH-MN had the best effect on promoting wound healing. A continuous epidermis and new blood vessels began to form on the skin surface, while the reduction of inflammatory cells and the formation of secondary skin elements (hair follicles and sebaceous glands) were also found. On day 21, compared with the other groups, the newly formed epithelial tissue of the ZGH-MN treatment group was similar to the normal skin tissue structure.

Second, Masson's trichrome staining and immunohistochemical staining were performed on the wound tissue to assess the arrangement and type of collagen during the healing process. As shown in Fig. 6, as the wound healed, the collagen fibers in the wound tissue of each group were gradually arranged in an orderly and directional manner, and the color change was gradually deepened. One can observe that the collagen fibers in the control and blank-MN treatment groups were discontinuous and disorganized. In the other experimental groups, the collagen fibers were intact, continuous, regular, and orderly, among which the ZGH-MN treatment group exhibited the most regular and orderly arrangement, similar to normal skin. This phenomenon implies that the physiological microcurrents generated by ZGH-MN have a facilitating effect on ECM deposition and collagen alignment during the wound-healing process.

The collagen fibers in the skin are mainly composed of types I and III collagen, of which type I collagen is thicker and plays an important role in supporting the hardness of the skin and making it firm. However, if its amount is too much, it will make the skin stiff, resulting in the formation of scars after the wound heals (*45*). Type III collagen is the main component of reticular fibers in the skin, and the higher the content of type III collagen, the finer the fiber bundle. In wound repair, the higher proportion of type III collagen, the more delicate and smooth the skin tissue (*46*). Therefore, to verify whether ZGH-MN can inhibit the formation of scars in the process of promoting wound healing, we conducted immunohistochemical staining of types I and III collagen in the 7 and 21 days' wound tissues. As shown in fig. S7, the ratio of type I/III collagen increased in all groups on day 7 due to the increase of type I collagen. The ZGH-MN, ZG-MN, and ZH-MN groups were significantly higher than the control, blank-MN, and ZIF-MN groups. On day 21, it was observed that the amount of type III collagen became higher, and type I collagen was reduced in the experimental group compared to the control group. The ratio of type I/III collagen in all experimental groups was lower than that of the control group. Among them, the type I/III collagen ratio in the ZGH-MN group was closer to the normal skin, indicating that the microcurrents generated from ZGH-MN can remodel the ECM and reduce scar formation in the later stages of wound healing.

Immunohistochemical analysis

An important reason for the difficulty of healing diabetic wounds is the persistent infection caused by a large number of inflammatory factors. To further investigate the inhibitory effect of conductive MN on the inflammatory response, we used immunohistochemical staining to quantify the levels of representative inflammatory cytokines in the healing wound tissue. It can be observed that on day 7, the levels of inflammatory factors such as interleukin-6 (IL-6), IL-1β, and tumor necrosis factor–α (TNF-α) were higher in the control group, while the levels of anti-inflammatory factors such as IL-4 and

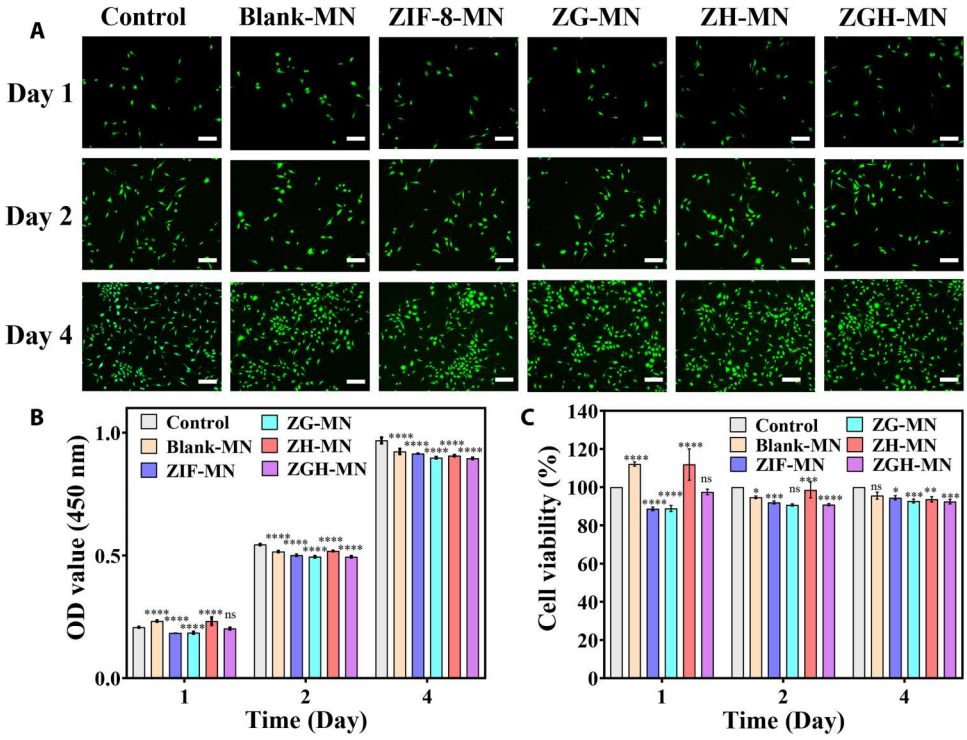

Fig. 4. Biocompatibility of the MN patches. (**A**) Live/dead cell staining images of L929 cells cultured with different samples after 1, 2, and 4 days. (**B** and **C**) OD values and the corresponding cell viability of different samples evaluated by the MTT test. ($n = 4$ per group; scale bars, 100 μm; *$P < 0.05$, **$P < 0.01$, ***$P < 0.001$, and ****$P < 0.0001$; ns, not significant.)

IL-13 were significantly lower (figs. S8 and S9). In contrast, the inflammatory factors of the treatment groups decreased, while the anti-inflammatory factors increased. The ZGH-MN group showed the most significant decrease in inflammatory factors such as IL-6, IL-1β, and TNF-α, with the corresponding highest levels of anti-inflammatory factors such as IL-4 and IL-13. On day 21, there was almost no sign of inflammation or infection in the ZGH-MN group, and only a small amount of IL-6, IL-1β, and TNF-α was expressed (Fig. 7), while the levels of anti-inflammatory factors such as IL-4 and IL-13 were also lower than those on day 7 (fig. S9). The above results showed that the control group had excessive inflammation, and the diabetic wound inflammation was reduced after MN treatment, among which the ZGH-MN patch treatment group had the least inflammatory response. The good anti-inflammatory effect of the ZGH-MN patch may be due to the fact that the MN patch can consume blood glucose on the surface of diabetic wounds to reduce the inflammatory response of the wound. On the other hand, it may be caused by the bioelectricity generated by the MN patch to inhibit the secretion of inflammatory factors IL-6, IL-1β, and TNF-α and up-regulate the secretion of anti-inflammatory factors IL-4 and IL-13.

The other important reason for the difficult healing of diabetic wounds is the high blood glucose concentration in the wound. Changes in local blood glucose concentration in wounds can be detected by the periodic acid–Schiff staining. As shown in fig. S10, on the seventh day, the wounds in all groups showed obvious purplish-red color, indicating that the wounds were at a high glucose level. On day 14, the ZGH-MN group showed a lighter purplish-red color compared with the control group and other treatment groups, indicating that the ZGH-MN patch could convert local glucose into gluconic acid through an enzyme-linked cascade reaction. This reduces the local level of blood glucose in the wound (Fig. 1B). On the 21st day, one could observe that the wounds in the control group, blank-MN, ZIF-MN, and ZH-MN group were still obviously purple-red, indicating that the wound surface was at a high glucose level. Compared with these groups, the ZG-MN and ZGH-MN groups had a lighter purple-red color. However, the effect of the ZGH-MN group was more obvious than that of the ZG-MN group, which indicates that the ZGH-MN patch could effectively reduce the local blood glucose concentration through the anode oxidation of BFCs to accelerate wound healing.

In the process of wound healing, keratinocytes regulate the activity of fibroblasts by secreting, activating, or inhibiting growth factors such as TGF-β, which play an important role in the formation of scars in the later stage of wound healing (*47*). To explore whether the conductive MN patch prepared in this study could prevent scar formation in the late stage of diabetic wound healing, we performed immunohistochemical staining for TGF-β on the healing wound tissue on day 21 (Fig. 7). The result showed that TGF-β was abundant and widely distributed in the control and other treatment groups; however, the production was significantly decreased in the ZGH-MN group, which suggests that the conductive ZGH-MN patch has the ability to inhibit excessive fibroblast production to prevent scar formation during the wound-healing process.

In addition, during the healing process of diabetic wounds, although new microvessels are essential to promote rapid wound healing, many studies in recent years have demonstrated that excessive angiogenesis can directly stimulate scarring (*48*). Therefore, we

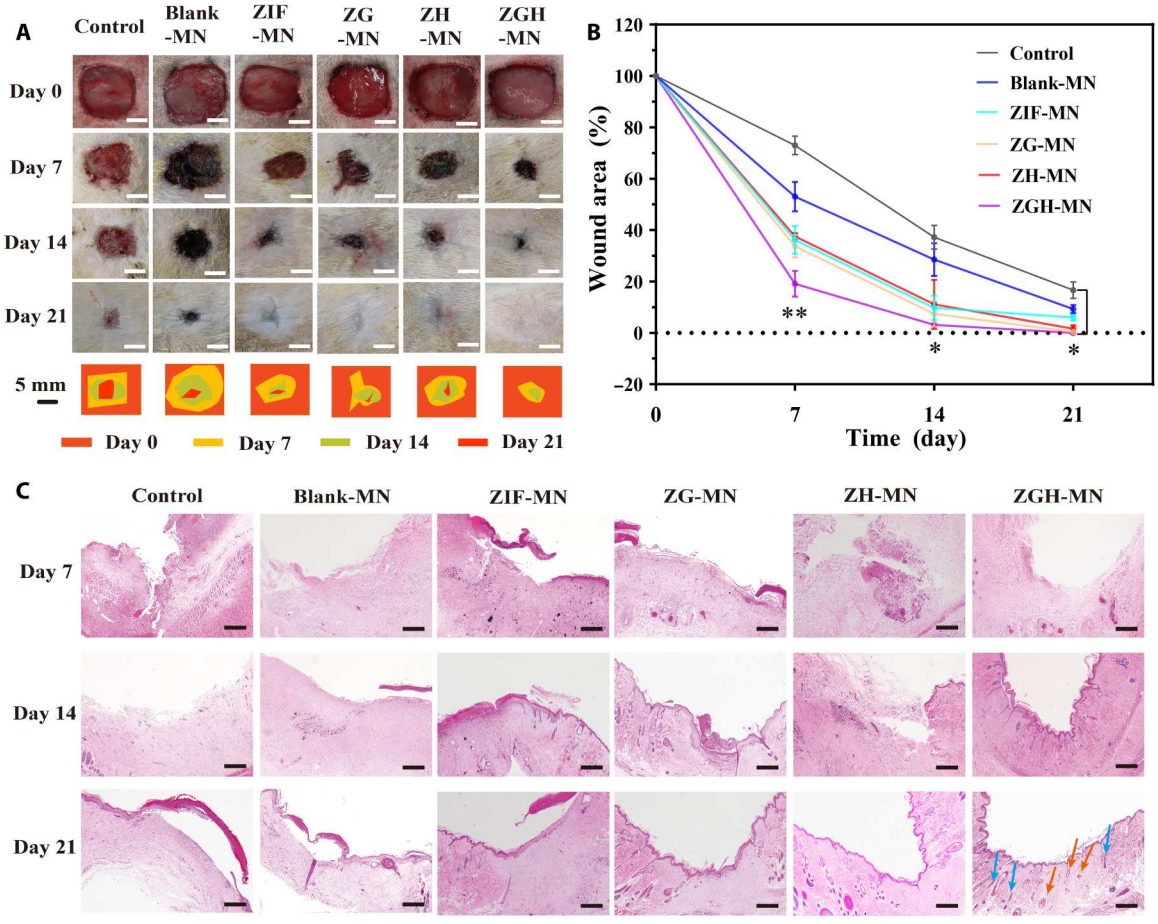

Fig. 5. The healing effect evaluation of the diabetic wound. (**A**) Animal wound healing by different MNs on days 0, 7, 14, and 21. (**B**) Quantitative analysis of the wound area after treatment with different samples (scale bars, 5 mm; *$P < 0.05$ and **$P < 0.01$). (**C**) Representative images of the H&E staining ($n = 3$ per group; scale bars, 200 μm; blue arrows, hair follicles; orange arrows, gland structure).

performed immunohistochemical staining for CD31, a marker of neovascularization on the healing wound tissue on days 7 and 21, to assess the effect of ZGH-MN on neovascularization during the wound process. As shown in Fig. 8A, on day 7, CD31 was significantly expressed in the experimental groups, especially in the ZGH-MN group, where its expression was much higher than that of the control group. This indicates that there is neovascularization at the wound site, which can promote rapid wound healing at an early stage. However, except for the control group, the expression level of CD31 in the wound site tissues of the experimental groups decreased on the 21st day, and the ZGH-MN patch treatment group had the lowest expression level, which indicates that the ZGH-MN patch was beneficial to prevent the formation of scar in the later stage of wound healing. Studies have shown that the timely denaturation of immature blood vessels in the process of wound healing is necessary to avoid the formation of scar tissue (*49*).

To further evaluate the effect of the self-powered enzyme-linked MN patch on preventing scar formation during diabetic wound healing, immunohistochemical staining was used to study the expressions of CD34 (a marker of hair follicle stem cells) and MMP9 (matrix metalloproteinases) at the wound site of the 21st day. As shown in Fig. 8B, the quantitative analysis results of CD34 were 0.6 ± 0.03% in the control group, 0.6 ± 0.02% in the blank-MN group, 1.3 ± 0.06% in the ZIF-MN group, 2.0 ± 0.04% in the ZG-MN group, 1.7 ± 0.05% in the ZH-MN group, and 4.0 ± 0.06% in the ZGH-MN group. The MMP9 quantitative analysis results were 3.5 ± 0.05% in the control group, 4.4 ± 0.06% in the blank-MN group, 4.7 ± 0.06% in the ZIF-MN group, 5.2 ± 0.06% in the ZG-MN group, 4.5 ± 0.04% in the ZH-MN group, and 6.0 ± 0.07% in the ZGH-MN group. The above results prove that the expression levels of CD34 and MMP9 in the experimental groups were much higher than those in the control group on day 21, and the expression levels in the ZGH-MN patch group were the highest. High expression levels of CD34 imply more regeneration of skin appendages (such as hair follicles), suggesting that the self-powered enzyme-linked MN patch can stimulate hair regeneration (validated by the H&E staining in Fig. 5B) and thus bring the skin tissue at the repaired wound site closer to normal skin tissue. The higher expression level of MMP9 in the ZGH-MN patch group indicates that the self-powered enzyme-linked MN patch could induce more active degradation of ECM, especially collagen I, during the remodeling stage of wound healing, thus inhibiting the formation of scar during wound healing (*50*).

The above study proves that the ZGH-MN patch can promote rapid healing of diabetic wounds and effectively prevent the formation of scars during the healing process caused by the bioelectricity

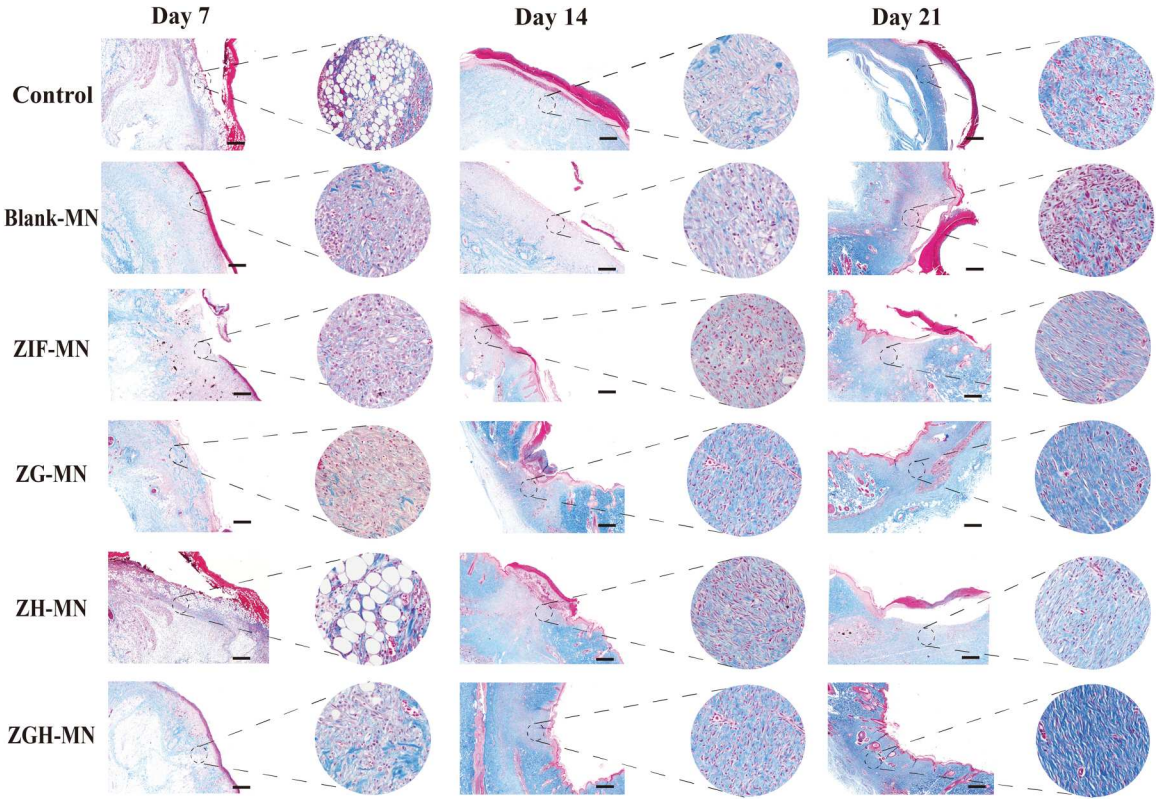

Fig. 6. Masson's trichrome staining of the healing wound tissues on days 7, 14, and 21 (scale bars, 200 μm).

generated from the ZGH-MN patch on the wound surface. As confirmed at the molecular level, bioelectricity can activate Smad2/3, phosphatidylinositol 3-kinase (PI3K), and nitric oxide synthase (NOS) pathways to regulate the expression of various growth factors such as TGF-β, epidermal growth factor (EGF), vascular endothelial growth factor (VEGF), and MMP9 (fig. S11) during the wound-healing process (*51*–*54*). The NOS pathway can regulate the secretion of pro-inflammatory factors (IL-1β, IL-6, and TNF-α) by M1 macrophages and anti-inflammatory factors (IL-4 and IL-13) by M2 macrophages, which is important for the inflammatory response during wound healing. The activation of the PI3K pathway can increase Ca^{2+} influx into cells, which in turn increases the phagocytosis of bacteria by macrophages and reduces the inflammatory response. In addition, the PI3K pathway can regulate angiogenesis, cell migration, and cell proliferation. The Smad2/3 pathway can regulate the ECM and thus affect cell production, apoptosis, and collagen fiber production. In summary, bioelectricity can regulate the inflammatory response, collagen deposition, cell proliferation, migration, and other wound-healing processes at the molecular level, so as to promote wound healing and prevent scar formation during the healing process.

In addition, another reason for the rapid healing of diabetic wounds treated by the ZGH-MN patch is to reduce the local blood glucose concentration around the wounds. The earlier studies confirmed that local hyperglycemia in diabetic wounds can produce high levels of reactive oxygen species (ROS) and induce the generation of advanced glycosylated end products (AGEs) (*55*). Hyperglycemia and the generation of AGEs will hinder the phagocytosis ability of macrophages to clear apoptotic neutrophils, resulting in the up-regulation of pro-inflammatory factors and down-regulation of anti-inflammatory factors, thus promoting the lasting pro-inflammatory state of diabetic wounds (*56*). High levels of ROS can keep the wound locally hypoxic, leading to a decrease in the levels of hypoxia induction factor-1, eventually down-regulating the expression of VEGF, as well as platelet-derived growth factor. Furthermore, hyperglycemia will cause a decrease in the number of bone marrow endothelial progenitor cells, which further affects wound angiogenesis (*57*, *58*). In addition to affecting inflammation and angiogenesis during wound healing, in the wound proliferation stage, AGEs can inhibit the proliferation of human dermal fibroblasts, and induce their apoptosis by activating the receptor for advanced glycation end products. Also, AGEs can inhibit the migration and adhesion of fibroblasts, keratinocytes, and endothelial cells. They will promote the aging of fibroblasts and hinder the normal healing of fibrosis, resulting in delayed healing of the diabetic wound (*57*). In conclusion, the ZGH-MN patch prepared in this study can reduce the local blood glucose in diabetic wounds, inhibit bacterial growth, inhibit IL-1β, IL-6, TNF-α, and other pro-inflammatory factors, and promote the secretion of IL-4, IL-13, and other anti-inflammatory factors, thus having a positive anti-inflammatory effect. In addition, ROS and AGEs can be adjusted to promote the generation of new blood vessels, as well as the proliferation and migration of cells in the process of wound healing (*58*, *59*), so as to promote rapid wound healing (fig. S12).

At present, natural polymers and their compounds with bioactive molecules are often used to treat wounds and prevent the

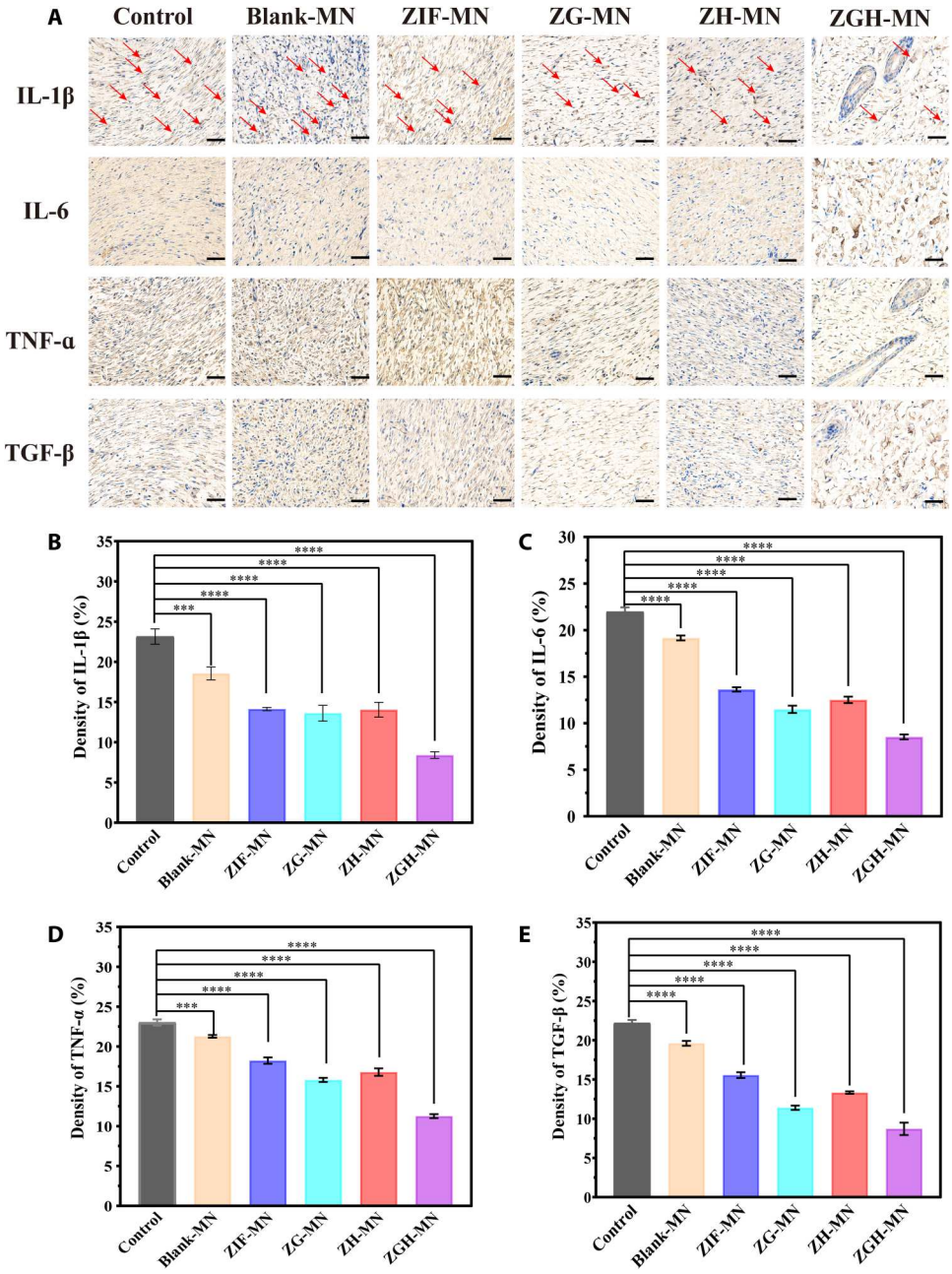

Fig. 7. Evaluation for inflammatory factors on the 21st day. (**A**) Immunohistochemistry staining for IL-1β, IL-6, TNF-α, and TGF-β on day 21. (scale bars, 20 μm; red arrows mark the positive regions). (**B** to **E**) Statistical analysis of IL-1β, IL-6, TNF-α, and TGF-β on day 21 (n = 3 per group. ***P < 0.001 and ****P < 0.0001.)

formation of scars (*60*). However, the wound-healing and scar-preventing effects of these materials were barely satisfactory owing to their relatively simple function. Compared to these materials, the MN developed in this study presented a more ideal wound healing and scar-preventing effect due to its multifunctionality, including the reduction in local hyperglycemia, antibacterial, anti-inflammation, and bioelectric simulation. However, our research lacks further verification of the scar-prevention characteristics of the ZGH-MN patch through scar animal model experiments, such as the rabbit ear scar model, which should be supplemented and improved in the follow-up research.

In summary, in this study, a self-powered enzyme-linked MN patch was designed and fabricated by combining the MN technology with an enzyme-linked BFC. The morphology, electrical conductivity, mechanical properties, antibacterial ability, and biocompatibility of the self-powered enzyme-linked MN patch were evaluated. The results show that the prepared MN tip has a complete shape, and after being applied to the diabetic wound of the rat, the evenly distributed ZG and ZH nanoparticles in the needle tip can rapidly undergo an enzymatic cascade reaction to reduce the local hyperglycemia of the wound. In general, the self-powered enzyme-linked MN patch not only can reduce the local

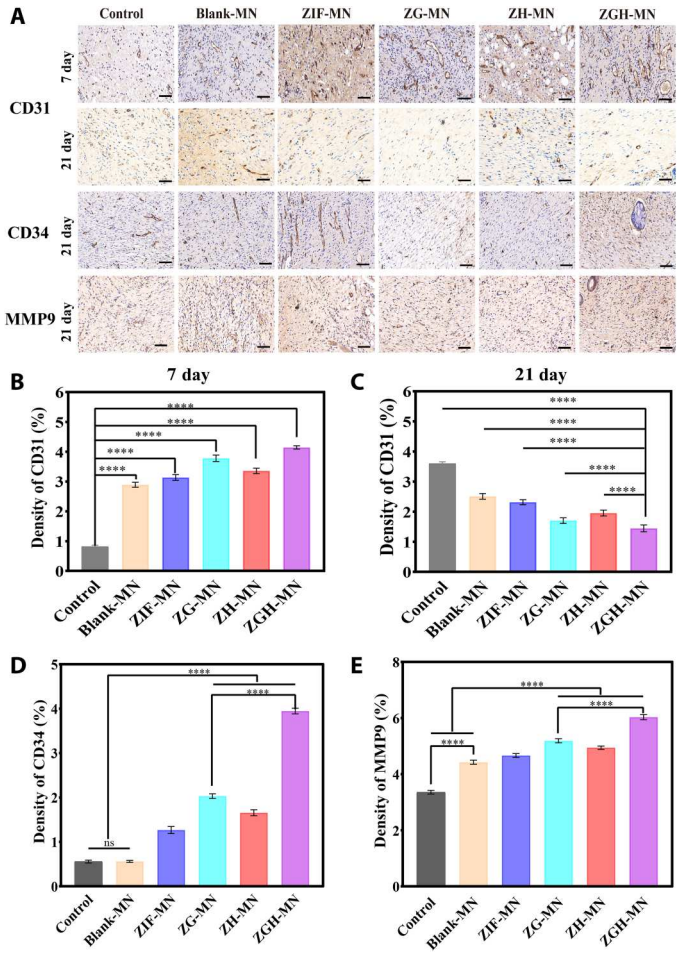

Fig. 8. Evaluation for CD31, CD34, and MMP9. (**A**) Immunohistochemistry staining for CD31, CD34, and MMP9 (CD31 on days 7 and 21; CD34 and MMP9 on day 21). (**B** and **C**) Quantitative analysis of CD31 on days 7 and 21. (**D** and **E**) Quantitative analysis of CD34 and MMP9 on day 21 ($n = 3$ per group; scale bars, 20 μm; ****$P < 0.0001$; ns, not significant).

blood glucose concentration and generate electrophysiological signals but also has high biocompatibility and antibacterial properties, which can quickly promote the healing of diabetic wounds and effectively prevent the formation of scar tissue, promising for applications in the field of diabetic wound repair.

MATERIALS AND METHODS

Materials

Sodium hyaluronate (HA, average molecular mass of 100 to 200 kDa), GOx, HRP, pyrrole, DA, RhB, H&E staining solution, and LB broth were purchased from Shanghai Macklin Biochemical Co. Ltd. Zinc nitrate hexahydrate [$Zn(NO_3)_2{\cdot}6H_2O$] and 2-methylimidazole were acquired from Aladdin. MTT, living/dead cell double-staining kit (calcein-AM/PI), and BCA protein assay kit were obtained from Dalian Meilun Biotechnology Co.

Preparation of DA-PPy

The synthesis of DA-functionalized PPy was achieved by the following procedures. Samples of 0.12 ml of pyrrole monomer and 0.01 g of DA hydrochloride were dissolved in 20.0 ml of 1.0 M HCl with continuous stirring at 0°C. Then $FeCl_3$/HCl solution (0.666 g/5 ml) was added to the mixed solution, which was stirred at 0°C for 6 hours. The precipitate was collected by centrifugation and washed with deionized (DI) water three times. The obtained precipitate was then freeze-dried for 24 hours to obtain the powder.

Preparation of ZG and ZH

For ZG synthesis, a mixture of $Zn(NO_3)_2{\cdot}6H_2O$ (40.0 mg), GOx (2.0 mg), and 2-methylimidazole (0.77 g) was dissolved in 5.0 ml of DI water and stirred at room temperature for 5 min. Subsequently, the reactive product was centrifuged to obtain ZG nanoparticles. As to ZH synthesis, the synthesis method was the same as ZG in addition to the weight of HRP, which was changed to 0.33 mg.

Enzyme packet rate detection

First, the protein standard solution was diluted to 0.025 to 2 mg/ml, and then reagents a and b were mixed thoroughly at a volume ratio of 50:1 to prepare the BCA working solution. The BCA working solution was stable within 24 hours at room temperature. Then, 20 μl of diluted protein standard solution, ZG/ZH supernatant, and 200 μl of BCA working solution of different concentrations were added to the 96-well cell culture plate in turn. After shaking for 30 s, the absorbance of the solution at 562 nm was recorded with a microplate reader. Last, a standard curve was plotted by taking the standard protein concentration as the abscissa and the absorbance value as the ordinate to obtain the linear relationship and the R^2 value. According to the formula obtained in the previous step, the entrapment rates of GOx and HRP in ZG/ZH nanoparticles were calculated.

Detection of enzyme cascade activity

Samples of 50 μl of glucose solution (1.00 mM) and 50 μl of TMB solution (1.25 mM) were added to 100 μl of ZG and ZH (2 mg/ml) solutions, and the mixed solution was incubated for 10 min. During this reaction, TMB was oxidized to a blue product (oxTMB) with UV absorption wavelengths of 370 and 652 nm, respectively. Then, 10 μl of H_2SO_4 solution (2.0 M) was added to the mixed solution to stop the color change; the blue product was converted into a yellow product with a UV absorbance of 450 nm.

Fabrication of MN patches

PVA/HA (w/w = 1/2), DA-PPy (w/v = 1%), and ZG/ZH (0.5 mg/ml) were mixed in DI water to prepare the tip solution. PVA/HA (w/w = 1/2) and DA-PPy (w/v = 1%) were dissolved in DI water to prepare the backing layer solution. The preparation process is illustrated in fig. S3. In detail, 50 μl of the ZG tip solution was added to one-half of the cavity of the standard conical MN molds (Blueacre Technology Ltd) and filled with vacuum-negative pressure. Likewise, another 50 μl of the ZH tip solution was added to the other half of the cavity of the MN template. Last, the backing layer solution was added to completely cover the tip, vacuumed again, and dried at 37°C for 12 hours. Last, the MNs can be obtained by demolding.

Characterization

The synthesized nanoparticles were characterized by TEM (Tecnai G2 F20 S-Twin, FEI, USA), the microstructures of the MN patch were characterized by the SEM (JSM-6701F, JEOL, Japan) after gold sputter coating. FTIR spectroscopy was performed on a

Bruker IFS66 V FTIR spectrophotometer. XRD patterns were recorded on a Rigaku D/Max-2400 diffractometer using Cu-Kα radiation and graphite monochromator (λ = 1.54056 Å). The fluorescent images of the RhB-loaded MNs were captured by a microscope (VERT1, Zeiss, Germany).

Mechanical strength test

MNs with different HA concentrations were placed on a horizontal specimen stage of an electronic tension testing machine (CMT2102, Zhejiang Think Eternal Technology Co. Ltd) one by one with their tips facing upward. The MNs were tested at a speed of 2 mm/min. The magnitude of the force on the MNs and the deformation of the needle tips were recorded.

Determination of the output current of the MN patch during the enzymatic cascade reaction

The prepared conductive MN patch was placed in a petri dish. Glucose solutions of different concentrations (0, 18, 20, 22, 24, 26 mM) were added dropwise every minute. The currents were measured with a high-precision benchtop digital multimeter (34461A, Keysight Technologies).

Study the correlation between the output current and the glucose consumption

The current output of the ZGH-MN patch in glucose solution with varying standard concentrations of 0, 0.5, 0.7, 0.9, 1.6, 2.0, 2.2, and 2.4 mM within 5 s was recorded. The average current values at different concentrations were then calculated. Using the GraphPad Prism software (Version 8.0.2), a linear regression equation was established to determine the relationship between the glucose consumed and current output.

Wound surface current test

The wound currents of the ZGH-MN patch were measured in full-thickness skin wounds of diabetic and normal rats. Adult male Wistar rats weighing 180 to 200 g were selected for animal experiments, with four rats in each group. The animal experiment process was approved by the Lanzhou University Animal Ethics Committee (LZUKQ-2021-051). Rats were first anesthetized with 10% (w/v) chloral hydrate (350 to 400 mg/kg), the dorsal hair was removed, and a 1 cm by 1 cm full-thickness wound was incised on the back of the rat. The ZGH-MN patch was fixed on the wound surface and connected with a high-precision desktop digital multimeter (34461A, Keysight Technologies).

Antibacterial ability

In the experiment, the antibacterial performance of the MNs was examined by the plate colony-counting method. First, the *E. coli* (ATCC 33525, Warner Bio) and *S. aureus* (ATCC 25923, Shanghai North Connaught Bio Technology Co. Ltd) were diluted in the active growth phase to 1×10^{-6}/ml. Next, different concentrations of ZIF-8, ZG, and ZH (0, 0.3, 0.5, and 1.0 mg/ml) nanoparticles were cocultured with equal volumes of the diluted bacterial solution at 37°C for 24 hours. Last, the cocultured bacterial solution was diluted again to 1×10^{-6}/ml and then inoculated into 200-μl agar plates. Photographs were taken after 24-hour incubation at 37°C and the number of surviving bacteria was counted by plate count.

When the antibacterial properties of different concentrations of nanoparticles were explored, we continued to study the antibacterial properties of MN patches prepared with nanoparticles (0.5 mg/ml) in the same manner as above.

In vitro cytotoxicity test

The cytotoxicity of the MN patch was evaluated by the MTT Assay. L929 cells (X120311, Shanghai Fusheng Industrial Co. Ltd., China) were divided into five groups and cocultured with different MNs of the same quality (blank-MN, ZIF-MN, ZG-MN, ZH-MN, and ZGH), in a 96-well plate for 4 days. Each group had triple parallels and the initial concentration of the cells in each well was 2×10^4 cells/ml. For the daily test, the materials were first transferred to sterile new wells, followed by the addition of 1.0 ml of culture medium with 10% MTT solution, and cocultured for 4 hours in the cell incubator. Last, the culture medium was removed and 400 μl of dimethyl sulfoxide was added to dissolve the formazan crystals. Cell viability for each group was acquired by measuring the corresponding optical density (OD) values.

The 2×10^4 L929 cells were cocultured with the same amount of different MNs for a certain period of time (1, 2, and 4 days). The cells were stained with a living/dead cell double-staining kit (Calcein-AM/PI) (100 μl per well) at room temperature for 30 min. Then, under an inverted fluorescence microscope, we observed the seeded live cells stained with green, while the dead cells stained with red, which was used to judge the effect of different MNs on the activity of L929 cells.

Establishment of the rat model

Fifty-four 6-week-old male Wistar rats (weighing about 180 to 200 g) were provided from the Animal Experiment Center of Lanzhou University. The animal experiment process was approved by the Lanzhou University Animal Ethics Committee (LZUKQ-2021-051).

The diabetic model was established by using STZ (10 mg/ml) through an intraperitoneal injection method (60 mg/kg). After that, the rats in the model group were forbidden to eat and drink for 12 hours. Three days later, when the blood glucose concentration of the rats was greater than 13.5 to 25 mM and the rats appeared listless, unresponsive, increased appetite, notably increased urine output, and lost weight, we could infer that the type 1 diabetes model was successfully established. The diabetic rats were anesthetized by intraperitoneal injection of 10% (w/v) chloral hydrate. Their backs were shaved and a rounded full-thickness cutaneous wound with a diameter of 1 cm was created.

In vivo animal experiment

The established animal models were randomly and equivalently divided into six groups, one of which was a control group, in which the rats received no treatments. The other five groups of diabetic rat wounds were treated with the blank-MN patch, ZIF-MN patch, ZG-MN patch, ZH-MN patch, and ZGH-MN patch, respectively. Everyday, the wounds of the rats were examined, and new MN patches were applied and fixed by their self-adhesive property, eliminating the need for additional auxiliary fixation methods. The diabetic wounds were recorded by taking photos on days 0, 7, 14, and 21. After that, the rats were euthanized, and the wound tissues were collected and fixed in a 4% paraformaldehyde buffer for 24 to 48 hours. The obtained tissue samples were then dehydrated, embedded in paraffin, and sectioned into 5- to 7-μm slices for further histology and immunohistochemistry analysis of CD31

(M15118, HUABIO), CD34 (14486-1-Ap, Proteintech), MMP9 (10375-2-Ap, Proteintech), collagen I (Affinity, AF7001), collagen III (Affinity, DF6087), IL-4 (bs-0581R, Bioss), IL-13 (IPB3854, Baijia), IL-6 (Affinity, DF6087), IL-1β (Affinity, AF5103), and TNF-α (Affinity, AF7014).

Statistical analysis

All data were expressed as mean ± standard deviation (SD) and analyzed by Origin Pro 2021 or GraphPad Prism. The difference between the treatment and control groups was assessed using the one-way analysis of variance (ANOVA) or two-way ANOVA, setting the level at $P < 0.05$ as statistical significance.

Supplementary Materials

This PDF file includes:

Figs. S1 to S12

View/request a protocol for this paper from *Bio-protocol*.

REFERENCES AND NOTES

1. P. A. Lazzarini, R. E. Pacella, D. G. Armstrong, J. J. van Netten, Diabetes-related lower-extremity complications are a leading cause of the global burden of disability. *Diabet. Med.* **5**, 1297–1299 (2018).
2. S. Patel, S. Srivastava, M. R. Singh, D. Singh, Mechanistic insight into diabetic wounds: Pathogenesis, molecular targets and treatment strategies to pace wound healing. *Biomed. Pharmacother.* **112**, 108615 (2019).
3. S. Liu, Q. Zhang, J. Yu, N. Shao, H. Lu, J. Guo, X. Qiu, D. Zhou, Y. Huang, Absorbable thioether grafted hyaluronic acid nanofibrous hydrogel for synergistic modulation of inflammation microenvironment to accelerate chronic diabetic wound healing. *Adv. Healthc. Mater.* **9**, e2000198 (2020).
4. A. Singh, S. Yadav, Microneedling: Advances and widening horizons. *Indian Dermatol. Online J.* **7**, 244–254 (2016).
5. L. Barnum, M. Samandari, T. A. Schmidt, A. Tamayol, Microneedle arrays for the treatment of chronic wounds. *Expert Opin. Drug Deliv.* **17**, 1767–1780 (2020).
6. S. Yao, Y. Wang, J. Chi, Y. Yu, Y. Zhao, Y. Luo, Y. Wang, Porous MOF microneedle array patch with photothermal responsive nitric oxide delivery for wound healing. *Adv. Sci.* **9**, 2103449 (2021).
7. M. Yin, J. Wu, M. Deng, P. Wang, G. Ji, M. Wang, C. Zhou, N. T. Blum, W. Zhang, H. Shi, N. Jia, X. Wang, P. Huang, Multifunctional magnesium organic framework-based microneedle patch for accelerating diabetic wound healing. *ACS Nano* **15**, 17842–17853 (2021).
8. X. Zhang, G. Chen, Y. Liu, L. Sun, L. Sun, Y. Zhao, Black phosphorus-loaded separable microneedles as responsive oxygen delivery carriers for wound healing. *ACS Nano* **14**, 5901–5908 (2020).
9. M. Monavarian, S. Kader, S. Moeinzadeh, E. Jabbari, Regenerative scar-free skin wound healing. *Tissue Eng. Part B Rev.* **25**, 294–311 (2019).
10. H. Sorg, D. J. Tilkorn, S. Hager, J. Hauser, U. Mirastschijski, Skin wound healing: An update on the current knowledge and concepts. *Eur. Surg. Res.* **58**, 81–94 (2017).
11. E. Wang, M. Zhao, Regulation of tissue repair and regeneration by electric fields. *Chin. J. Traumatol.* **13**, 55–61 (2010).
12. J. M. Rhett, G. S. Ghatnekar, J. A. Palatinus, M. O'Quinn, M. J. Yost, R. G. Gourdie, Novel therapies for scar reduction and regenerative healing of skin wounds. *Trends Biotechnol.* **26**, 173–180 (2008).
13. B. Tandon, J. J. Blaker, S. H. Cartmell, Piezoelectric materials as stimulatory biomedical materials and scaffolds for bone repair. *Acta Biomater.* **73**, 1–20 (2018).
14. J. Jacob, N. More, K. Kalia, G. Kapusetti, Piezoelectric smart biomaterials for bone and cartilage tissue engineering. *Inflamm. Regen.* **38**, 2 (2018).
15. A. H. Rajabi, M. Jaffe, T. L. Arinzeh, Piezoelectric materials for tissue regeneration: A review. *Acta Biomater.* **24**, 12–23 (2015).
16. B. Tandon, A. Magaz, R. Balint, J. J. Blaker, S. H. Cartmell, Electroactive biomaterials: Vehicles for controlled delivery of therapeutic agents for drug delivery and tissue regeneration. *Adv. Drug Deliv. Rev.* **129**, 148–168 (2018).
17. J. Liang, H. Zeng, L. Qiao, H. Jiang, Q. Ye, Z. Wang, B. Liu, Z. Fan, 3D printed piezoelectric wound dressing with dual piezoelectric response models for scar-prevention wound healing. *ACS Appl. Mater. Interfaces* **14**, 30507–30522 (2022).
18. X. Xiao, The direct use of enzymatic biofuel cells as functional bioelectronics. *eScience* **2**, 1–9 (2022).
19. J. R. Sempionatto, J. Wang, On-body bioelectronics: Wearable biofuel cells for bioenergy harvesting and self-powered biosensing. *Adv. Funct. Mater.* **30**, 1906243 (2020).
20. H. Kai, T. Yamauchi, Y. Ogawa, A. Tsubota, T. Magome, T. Miyake, K. Yamasaki, M. Nishizawa, Accelerated wound healing on skin by electrical stimulation with a bioelectric plaster. *Adv. Healthc. Mater.* **6**, 1700465 (2017).
21. J. Kim, I. Jeerapan, J. R. Sempionatto, A. Barfidokht, R. K. Mishra, A. S. Campbell, L. J. Hubble, J. Wang, Wearable bioelectronics: Enzyme-based body-worn electronic devices. *Acc. Chem. Res.* **51**, 2820–2828 (2018).
22. H. Chen, Y. Cheng, J. Tian, P. Yang, X. Zhang, Y. Chen, Y. Hu, J. Wu, Dissolved oxygen from microalgae-gel patch promotes chronic wound healing in diabetes. *Sci. Adv.* **6**, eaba4311 (2020).
23. C. Hou, Y. Wang, Q. Ding, L. Jiang, M. Li, W. Zhu, D. Pan, H. Zhu, M. Liu, Facile synthesis of enzyme-embedded magnetic metal–organic frameworks as a reusable mimic multi-enzyme system: Mimetic peroxidase properties and colorimetric sensor. *Nanoscale* **7**, 18770–18779 (2015).
24. S. S. Nadar, V. K. Rathod, Magnetic-metal organic framework (magnetic-MOF): A novel platform for enzyme immobilization and nanozyme applications. *Int. J. Biol. Macromol.* **120**, 2293–2302 (2018).
25. S. S. Nadar, L. Vaidya, V. K. Rathod, Enzyme embedded metal organic framework (enzyme-MOF): De novo approaches for immobilization. *Int. J. Biol. Macromol.* **149**, 861–876 (2020).
26. K. S. Park, Z. Ni, A. P. Côté, J. Y. Choi, R. Huang, F. J. Uribe-Romo, H. K. Chae, M. O'Keeffe, O. M. Yaghi, Exceptional chemical and thermal stability of zeolitic imidazolate frameworks. *Proc. Natl. Acad. Sci. U.S.A.* **103**, 10186–10191 (2006).
27. J. Zhang, Y. Tan, W.-J. Song, Zeolitic imidazolate frameworks for use in electrochemical and optical chemical sensing and biosensing: A review. *Microchim. Acta.* **187**, 234 (2020).
28. T.-T. Chen, J.-T. Yi, Y.-Y. Zhao, X. Chu, Biomineralized metal-organic framework nanoparticles enable intracellular delivery and endo-lysosomal release of native active proteins. *J. Am. Chem. Soc.* **140**, 9912–9920 (2018).
29. H. Chen, J. Yang, L. Sun, H. Zhang, Y. Guo, J. Qu, W. Jiang, W. Chen, J. Ji, Y. W. Yang, B. Wang, Synergistic chemotherapy and photodynamic therapy of endophthalmitis mediated by zeolitic imidazolate framework-based drug delivery systems. *Small* **15**, e1903880 (2019).
30. Z. Yang, Y. Qian, F. Yang, C. Chen, X. Tang, J. Jin, Investigating adsorption/desorption of DNA on ZIF-8 surface by fluorescently labeled oligonucleotides. *Langmuir* **35**, 16290–16296 (2019).
31. Z. Zhou, Z. Gao, H. Shen, M. Li, W. He, P. Su, J. Song, Y. Yang, Metal-organic framework in situ post-encapsulating DNA-enzyme composites on a magnetic carrier with high stability and reusability. *ACS Appl. Mater. Interfaces* **12**, 7510–7517 (2020).
32. M. Taheri, D. Ashok, T. Sen, T. G. Enge, N. K. Verma, A. Tricoli, A. Lowe, D. R. Nisbet, T. Tsuzuki, Stability of ZIF-8 nanopowders in bacterial culture media and its implication for antibacterial properties. *Chem. Eng. J.* **413**, 127511 (2021).
33. S. Yao, J. Chi, Y. Wang, Y. Zhao, Y. Luo, Y. Wang, Zn-MOF encapsulated antibacterial and degradable microneedles array for promoting wound healing. *Adv. Healthc. Mater.* **10**, e2100056 (2021).
34. A. Mihic, Z. Cui, J. Wu, G. Vlacic, Y. Miyagi, S.-H. Li, S. Lu, H.-W. Sung, R. D. Weisel, R.-K. Li, A conductive polymer hydrogel supports cell electrical signaling and improves cardiac function after implantation into myocardial infarct. *Circulation* **132**, 772–784 (2015).
35. N. Sahiner, S. Demirci, The use of p(4-VP) cryogel as template for in situ preparation of p(An), p(Py), and p(Th) conductive polymer and their potential sensor applications. *Synthetic Met.* **227**, 11–20 (2017).
36. W. Zhang, Y. Zhou, K. Feng, J. Trinidad, A. Yu, B. Zhao, Morphologically controlled bio-inspired dopamine-polypyrrole nanostructures with tunable electrical properties. *Adv Electron Mater.* **1**, 1500205 (2015).
37. C. Zhang, L. Zhang, W. Wu, F. Gao, R.-Q. Li, W. Song, Z.-N. Zhuang, C.-J. Liu, X.-Z. Zhang, Artificial super neutrophils for inflammation targeting and HClO generation against tumors and infections. *Adv. Mater.* **31**, e1901179 (2019).
38. X. Yang, L. Qiu, X. Luo, ZIF-8 derived Ag-doped ZnO photocatalyst with enhanced photocatalytic activity. *RSC Adv.* **8**, 4890–4894 (2018).
39. S. Li, E. Pang, C. Gao, Q. Chang, S. Hu, N. Li, Cerium-mediated photooxidation for tuning pH-dependent oxidase-like activity. *Chem. Eng. J.* **397**, 125471 (2020).
40. L. Gao, J. Zhuang, L. Nie, J. Zhang, Y. Zhang, N. Gu, T. Wang, J. Feng, D. Yang, S. Perrett, X. Yan, Intrinsic peroxidase-like activity of ferromagnetic nanoparticles. *Nat. Nanotechnol.*. **2**, 577–583 (2007).
41. H. Wang, C. Liu, Z. Liu, J. Ren, X. Qu, Specific oxygenated groups enriched graphene quantum dots as highly efficient enzyme mimics. *Small* **14**, 1703710 (2018).
42. L. Tang, S. J. Chang, C.-J. Chen, J.-T. Liu, Non-invasive blood glucose monitoring technology: A Review. *Sensors (Basel).* **20**, 6925 (2020).

43. Z. Zhu, H. Luo, W. Lu, H. Luan, Y. Wu, J. Luo, Y. Wang, J. Pi, C. Y. Lim, H. Wang, Rapidly dissolvable microneedle patches for transdermal delivery of exenatide. *Pharm. Res.* **31**, 3348–3360 (2014).
44. M. Chang, T. T. Nguyen, Strategy for treatment of infected diabetic foot ulcers. *Acc. Chem. Res.* **54**, 1080–1093 (2021).
45. F. A. G. da Silva Jr, J. C. Queiroz, E. R. Macedo, A. W. C. Fernandes, N. B. Freire, M. M. da Costa, H. P. de Oliveira, Antibacterial behavior of polypyrrole: The influence of morphology and additives incorporation. *Mat Sci Eng: C.* **62**, 317–322 (2016).
46. E. Davison-Kotler, W. S. Marshall, E. García-Gareta, Sources of collagen for biomaterials in skin wound healing. *Bioengineering (Basel).* **6**, 56 (2019).
47. L. Cuttle, M. Nataatmadja, J. F. Fraser, M. Kempf, R. M. Kimble, M. T. Hayes, Collagen in the scarless fetal skin wound: Detection with picrosirius-polarization. *Wound Repair Regen.* **13**, 198–204 (2005).
48. S. M. Karppinen, R. Heljasvaara, D. Gullberg, K. Tasanen, T. Pihlajaniemi, Toward understanding scarless skin wound healing and pathological scarring. *F1000Res.* **8**, F1000 Faculty Rev-787 (2019).
49. L. A. DiPietro, Angiogenesis and wound repair: When enough is enough. *J. Leukoc. Biol.* **100**, 979–984 (2016).
50. S. Korntner, C. Lehner, R. Gehwolf, A. Wagner, M. Grütz, N. Kunkel, H. Tempfer, A. Traweger, Limiting angiogenesis to modulate scar formation. *Adv. Drug Deliver. Rev.* **146**, 170–189 (2019).
51. K. Wu, M. Fu, Y. Zhao, E. Gerhard, Y. Li, J. Yang, J. Guo, Anti-oxidant anti-inflammatory and antibacterial tannin-crosslinked citrate-based mussel-inspired bioadhesives facilitate scarless wound healing. *Bioact. Mater.* **20**, 93–110 (2023).
52. J.-J. Lee, H. Y. Ng, Y.-H. Lin, E.-W. Liu, T.-J. Lin, H.-T. Chiu, X.-R. Ho, H.-A. Yang, M.-Y. Shie, The 3D printed conductive grooved topography hydrogel combined with electrical stimulation for synergistically enhancing wound healing of dermal fibroblast cells. *Biomater. Adv.* **142**, 213132 (2022).
53. M. Zhao, J. Penninger, R. R. Isseroff, Electrical activation of wound-healing pathways. *Adv. Skin Wound Care* **1**, 567–573 (2010).
54. K. Katoh, Effects of electrical stimulation of the cell: Wound healing, cell proliferation, apoptosis, and signal transduction. *Med. Sci. (Basel).* **11**, 11 (2023).
55. Y. Wang, M. Rouabhia, Z. Zhang, Pulsed electrical stimulation benefits wound healing by activating skin fibroblasts through the TGFβ1/ERK/NF-κB axis. *Biochim. Biophys. Acta* **1860**, 1551–1559 (2016).
56. S. Matoori, A. Veves, D. J. Mooney, Advanced bandages for diabetic wound healing. *Sci. Transl. Med.* **13**, eabe4839 (2021).
57. S. L. Wong, M. Demers, K. Martinod, M. Gallant, Y. Wang, A. B. Goldfine, C. R. Kahn, D. D. Wagner, Diabetes primes neutrophils to undergo NETosis, which impairs wound healing. *Nat. Med.* **21**, 815–819 (2015).
58. W. Qi, C. Yang, Z. Dai, D. Che, J. Feng, Y. Mao, R. Cheng, Z. Wang, X. He, T. Zhou, X. Gu, L. Yan, X. Yang, J.-X. Ma, G. Gao, High levels of pigment epithelium-derived factor in diabetes impair wound healing through suppression of Wnt signaling. *Diabetes* **64**, 1407–1419 (2015).
59. G. K. Kolluru, S. C. Bir, C. G. Kevil, Endothelial dysfunction and diabetes: Effects on angiogenesis, vascular remodeling, and wound healing. *Int. J. Vasc. Med.* **2012**, 918267 (2012).
60. X.-Y. Ji, Y. Chen, G.-H. Ye, M.-W. Dong, K.-Z. Lin, J.-G. Han, X.-P. Feng, X.-B. Li, L.-S. Yu, Y.-Y. Fan, Detection of RAGE expression and its application to diabetic wound age estimation. *Int. J. Leg. Med.* **131**, 691–698 (2017).

Acknowledgments: We thank Key Laboratory of Dental Maxillofacial Reconstruction and Biological Intelligence Manufacturing, Gansu Province for providing the experimental platform. **Funding:** This work was supported by the National Natural Science Foundation of China (82272500 and 81571829), the Natural Science Foundation of Gansu Province (20JR10RA597), the Fundamental Research Funds for the Central Universities (lzujbky-2021-ct08 and lzujbkj-2021-kb27), the Open Project of State Key Laboratory of Solid Lubrication, and the Lanzhou Institute of Chemical Physics, Chinese Academy of Sciences (LSL-1907), the Open Subject Foundation of Key Laboratory of Dental Maxillofacial Reconstruction and Biological Intelligence Manufacturing (20JR10RA653-ZDKF20210101), and the Medical Innovation and Development Project of Lanzhou University. **Author contributions:** Conceptualization: Z.F. Methodology: X.Z. Investigation: X.Z., Z.W., and H.J. Visualization: X.Z., Z.W., H.J., H.Z., and N.A. Supervision: Z.F. Writing (original draft): X.Z. and Z.W. Writing (review and editing): L.S., B.L., and Z.F. **Competing interests:** The authors declare that they have no competing interests. **Data and materials availability:** All data needed to evaluate the conclusions in the paper are present in the paper and/or the Supplementary Materials.

Submitted 14 February 2023
Accepted 14 June 2023
Published 14 July 2023
10.1126/sciadv.adh1415